FINAL TECHNICAL REPORT

for

NASA Grant NSG-7565

ANALYSIS OF VIKING INFRARED THERMAL MAPPING DATA OF MARS.

Duane O. Muhleman

Principal Investigator

Division of Geological and Planetary Sciences

California Institute of Technology

Pasadena, California 91125

Grant Period

October 1, 1978 - September 30, 1979

ANALYSIS OF VIKING INFRARED THERMAL MAPPING DATA OF MARS

Variations in the thermal inertia on Mars occur spatially, with values ranging from about 1.5 to 16 (units of 10^{-3} cal/cm^{2}s$^{\frac{1}{2}}$K) (Kieffer et al. 1977). These are often interpreted in terms of the average particle size of the surface (Kieffer et al. 1973). Pictures returned from the surface, however, show that there are complications to this simplistic view, including rocks and fines on the same surface, atmospheric dust, surface slopes, condensable CO_2, layering of materials (such as fines overlying solid rock), and changes in elevation. Additionally, there is evidence in the surface temperatures observed by the Viking Infrared Thermal Mapper that the simple approach cannot explain. This includes a post-dawn warming and a late-afternoon cooling of the surface relative to the temperatures predicted by the simple model.

The various non-ideal types of surfaces were modeled numerically to predict their thermal behavior. Apparent thermal inertias of various surfaces were determined, and the diurnal temperature variation examined.

It was found that the apparent inertia increases with increased surface rock abundance or with increasing atmospheric dust. Additionally, it was found that these surfaces all produced diurnal temperature behavior similar to that observed, including specifically the rapid afternoon cooling. The afternoon cooling observed at the Viking Lander-1 site (Kieffer et al. 1976) is capable of being explained by the non-ideal model for the area, while that atop Arsia Mons volcano is not. This latter effect may be due to the observing geometry.

A histogram of thermal inertia versus elevation shows some interesting effects. One class of surface, extending from high inertias at low elevations to low inertias at high elevations, is understandable almost solely in terms of the variation expected due to the differing amounts of atmospheric dust. Another grouping at low elevations, with low inertias, likely represents a distinct surface. Of course, within both of these groups occur large variations in inertia, presumably related to variations in surface particle size of fractional rock cover.

The results of this investigation are presented in a paper by B.M. Jakosky, entitled "The Effects of Non-Ideal Surfaces on the Derived Thermal Properties of Mars," to be published in the 30 December, 1979, issue of the Journal of Geophysical Research.

REFERENCES

Kieffer, H.H., S.C. Chase, E.D. Miner, G. Münch, and G. Neugebauer, Preliminary Report on Infrared Radiometric Measurements from the Mariner 9 Spacecraft, J. Geophys. Res., 78, 4291-4312, 1973.

Kieffer, H.H., S.C. Chase, Jr., E.D. Miner, F.D. Palluconi, G. Münch. G. Neugebauer, and T.Z. Martin, Infrared Thermal Mapping the the Martian Surface and Atmosphere: First Results, Science, 193, 780-786, 1976.

Kieffer, H.H., T.Z. Martin, A.R. Peterfruend, B.M. Jakosky, E.D. Miner, and F.D. Palluconi, Thermal and Albedo Mapping of Mars During the Viking Primary Mission, J. Geophys. Res., 82, 4249-4291, 1977.

THE EFFECTS OF NON-IDEAL SURFACES ON THE DERIVED THERMAL PROPERTIES OF MARS

BRUCE M. JAKOSKY

Division of Geological and Planetary Sciences

California Institute of Technology

Pasadena, California 91125

Running Title: Mars: Thermal Inertias and Non-Ideal Properties

Contribution Number 3228 of the Division of Geological and Planetary Sciences, California Institute of Technology, Pasadena, CA 91125.

ABSTRACT

The thermal intertia of the surface of Mars varies spatially by a factor of eight. This is attributable to changes in the average particle size of the fine material, the surface elevation, the atmospheric opacity due to dust, and the fraction of the surface covered by rocks and fine material. The effects of these non-ideal properties on the surface temperatures and derived thermal inertias are modeled, along with the effects of slopes, CO_2 condensed onto the surface, and layering of fine material upon solid rock. The non-ideal models are capable of producing thermal behavior similar to that observed by the Viking Infrared Thermal Mapper, including a morning delay in the post-dawn temperature rise and an enhanced cooling in the afternoon relative to any ideal, homogeneous model. The enhanced afternoon cooling observed at the Viking-1 landing site is reproduced by the non-ideal models while that atop Arsia Mons volcano is not, but may be attributed to the observing geometry. A histogram of surface thermal inertia versus elevation shows at least two distinct classes: a single region near Amazonis Planitia has low inertias at low elevations; much of the remaining data shows an anti-correlation between inertia and elevation, expected because of the change in thermal inertia produced by changes in the atmospheric pressure and dust opacity with elevation.

I. INTRODUCTION

The thermal inertias of various regions of Mars have been determined by Kieffer et al. (1977) based on infrared measurements of surface brightnesses obtained from the Viking Orbiter Infrared Thermal Mapping (IRTM) experiment. Thermal inertia can be interpreted as a gross measure of surface material average particle size (Kieffer et al., 1973, 1977). The purpose of this work is to examine the effects on the observed brightness temperatures and the derived thermal inertias of some of the non-ideal properties of the Martian surface. These include mixing at the surface of different materials (such as dust and rock), slopes on the surface, CO_2 frost condensing out at night, and dust in the atmosphere.

The thermal inertia of a material is defined by $I = \sqrt{K\rho C}$, where K is the thermal conductivity, ρ is the density, and C is the specific heat of the material. Along with the albedo A (the ratio of energy reflected to that incident at the surface), the thermal inertia controls the diurnal behavior of the surface temperatures. Although there are other dependences, to first order I determines the diurnal temperature amplitude while A controls the average surface temperature (e.g., Kieffer et al., 1973).

The thermal inertia of a planetary surface is obtained remotely by matching infrared brightness temperatures observed over the day to those predicted by a thermal model with various surface thermal properties. This has been done for the earth (e.g., Gillespie and Kahle, 1977), the

Moon (e.g., Jaeger, 1953; Winter and Saari, 1969), Mercury (Chase et al., 1976), and Mars (Kieffer et al., 1973, 1977). Values obtained range from an I of about 1. x 10^{-3} cal-$cm^{-\frac{1}{2}}$ - $s^{-\frac{1}{2}}$ - K^{-1} (hereafter referred to as an inertia of 1., with the units 10^{-3} cal-cm^{-2} - $s^{-\frac{1}{2}}$ - K^{-1} understood) for the fine particulate material of the Moon (Winter and Saari, 1969), to an I of about 60 for solid rock (Carslaw and Jaeger, 1959, p. 497). The average thermal inertia on Mars is 6.5 (Kieffer et al., 1973), with values ranging from about 1.6 to 12 (Kieffer et al., 1977).

The change in temperature of an ideal (i.e., flat, uniform, and homogeneous) surface during the day is dependent on the thermal skin depth of the material, given by $\ell_t = \sqrt{\frac{K}{\rho C}\frac{P}{\pi}}$, where P is the period of the insolation variation. A low inertia material with low conductivity will have a smaller skin depth, and hence a larger diurnal temperature variation than a higher inertia material. For the moon, measurements of temperature variation during a lunar eclipse, with its shorter period than a lunation, provide values of the thermal inertia over a smaller depth than do measurements over a lunation. Discrepancies between the lunation and eclipse measurements have been resolved using a depth-dependent conductivity or surface layering (Winter and Saari, 1969; Ingrao et al., 1966).

For Mars, non-ideal models are required based on other evidence in the data. These include an enhanced afternoon cooling of the Martian surface relative to the homogeneous thermal model predictions; a delay in post-dawn response to the sun relative to the model; differences between the brightness temperatures observed at different wavelengths; the unexpectedly wide range of thermal inertias observed on the planet; and the surface inhomogeneties observed directly by the Viking landers.

The afternoon cooling, first noted in the Mariner 9 radiometer data by Kieffer et al. (1973), involves surface temperatures in the late afternoon which are up to 30 K cooler than those predicted from the homogeneous model which best fits the predawn and morning temperatures (Fig. 1). The magnitude of this effect at the VL-1 landing site was about 6 K during the Viking primary mission (Kieffer et al., 1976a). As will be shown, an afternoon cooling similar to that observed will occur as a result either of dust in the atmosphere or a mixing of surface materials. It can also be caused by surface roughness if the cool, shaded sides of relief features are preferentially observed.

A delay in the rise of the surface temperatures after sunrise is seen in some locales, especially near the Tharsis volcanoes. This has been attributed to the presence of CO_2 frost over parts of the surface, condensing out of the atmosphere at night and subliming some time after sunrise (Kieffer et al., 1976b). When the frost is present on the surface after sunrise, the average surface brightness temperatures will be depressed relative to a frost-free surface, accounting for the delay.

Self-consistent, systematic differences between the brightness temperatures at the different IRTM passbands are observed (Fig. 2; Martin et al., 1979). The instrument observes in thermal infrared bands centered at 7, 9, 11, 15, and 20 μm in addition to a broadband visual channel (Chase et al., 1978; Kieffer et al., 1977).

The 15-μm channel is centered on the CO_2 absorption band and sees only the atmosphere, but the other infrared channels sense radiation emitted mostly from the surface. Real differences between the brightness temperatures at the different wavelengths can be caused by several possible mechanisms. A gray-body emissivity or a wavelength-dependent emissivity will cause spectral differences. They can also be due to differing amounts of absorption and emission by the atmosphere or the dust or clouds therein (Hunt, 1979). Finally, they may be caused by anisothermalities on the surface (areal mixtures of materials with different temperatures), as might be caused by mixtures of dust and rock, surface slopes in different directions, or CO_2 frost covering only parts of the surface. While dust and ice clouds are probably responsible for most of the differences (Martin et al., 1979: Hunt, 1979), Anisothermalities can create large spectral contrasts. Determinations of the infrared optical thickness of the atmosphere depend on these contrasts (Martin et al., 1979), as do the derivations of cloud composition and properties (Hunt, 1979). Spectral contrasts caused by spatial variations in surface composition (e.g., Hunt and Vincent, 1968) cannot be predicted a priori.

The thermal inertia on Mars, as mapped at a scale of 2° in latitude by 2° in longitude (about 120 km square at the equator) by Kieffer et al. (1977), varies spatially by as much as a factor of eight. The change in inertia from place to place can be caused by changes in the particle size of a uniform homogeneous surface, from less than 0.01 cm to 0.5 cm

(Kieffer et al., 1973); changes in the surface elevation, with the conductivity due to the interstitial gases varying to change the thermal inertia (e.g., Wechsler et al., 1972) and the different amounts of dust and downward-going atmospheric radiation above the surface changing the apparent inertia; changes in the fraction of the surface covered by solid rock; or combinations of these properties.

A final reason for determining the effects of non-ideal surfaces is that they in fact occur on Mars. Rocks, slopes and frosts are observed at the surface (Mutch et al., 1976; Jones et al., 1979), and dust is seen in the atmosphere (Pollack et al., 1977, 1979; Thorpe, 1977).

The next section of this paper discusses the thermal models used for calculating the temperatures of the ideal and non-ideal surfaces. In the third section, the surface temperatures and derived thermal inertias for the various non-ideal surfaces are presented. The fourth section shows the application of these models to the surface of Mars, discussing the VL-1 landing site, the caldera atop Arsia Mons volcano, and the global relationships between thermal inertia and surface elevation. The final section summarizes the results.

II. The Thermal Models

The effects of various non-ideal surfaces on the thermal characteristics of the surface of the planet can be determined by comparing the diurnal temperature variations appropriate for a surface containing the non-ideal traits to those for the ideal surface. The daily temperature profile of each surface is obtained using an iterative finite-differencing solution to the thermal diffusion equation, with the appropriate boundary conditions applied.

For the ideal homogeneous surface, the thermal diffusion equation,

$$\frac{\partial T}{\partial t} = \frac{K}{\rho C} \frac{\partial^2 T}{\partial Z^2} \qquad (1)$$

where

T temperature

t time

Z depth beneath the surface,

is solved iteratively by computer, with the boundary conditions of no heat flow at depth and of conservation of energy at the surface. The latter condition is:

$$\frac{S_\odot}{R^2} (1 - A) \cos i + I \left.\frac{\partial T}{\partial Z'}\right|_{Z' = 0} + F_a + L \frac{dm}{dt} = \epsilon \sigma T^4 \qquad (2)$$

where

$S_\odot$ solar constant

R Mars heliocentric distance

i solar incidence angle

Z' Z/ℓ_t, the depth normalized to the thermal skin depth

F_a down-going energy flux from the atmosphere

L latent heat of CO_2 frost formation

m mass of CO_2 present on the surface

ϵ surface emissivity

σ Stefan-Boltzmann constant

The model is identical to that used by Kieffer et al. (1977; Appendix I), except for the absence here of a seasonal memory. Instead, the temperature iterations continue with constant sun-Mars geometry until the solution converges, generally requiring several model days' calculations.

In detail, the model consists of twelve depth layers, extending down to 5.2 ℓ_t. The surface layer is 0.15 ℓ_t thick, and each successive layer increases in thickness by a factor of 1.2. The minimum iteration time step is 1/384 Martian day and increases by factors of two at depth where permitted by the convergence criteria.

The ideal model assumes thermal properties that are constant with depth. The nominal density and specific heat assumed are 1.5 g/cm^3 and 0.2 $cal\text{-}g^{-1}\text{-}K^{-1}$ respectfully, so that $\rho C = 0.3\ cal - K^{-1} - cm^{-3}$. Any variations in thermal inertia are obtained by varying K rather than ρ or C, because K will vary orders of magnitude more among candidate surface materials than ρ or C (Wechsler et al., 1972). However, the surface temperature of an ideal surface depends only on the value of $\sqrt{K\rho C}$, and not on any of the individual values.

The temperature-dependences of the thermal conductivity and specific heat are ignored in the models (see later in this section). In the ideal model, sunlight is assumed transmitted through the atmosphere unattenuated. The atmospheric radiation to the surface, due to absorption by the atmospheric CO_2 of emitted thermal radiation, is taken as 0.02 of the noon-time solar flux. The surface is treated as a blackbody, with unit emissivity. The surface temperature every 1/48 Martian day is saved for analysis.

CO_2 can condense onto the surface whenever the surface would otherwise drop below the condensation temperature appropriate for the surface atmospheric pressure. At the mean surface pressure of 6.2 mbar, this occurs at about 148 K, while at the pressure at the summits of the large volcanoes, condensation begins at about 133 K. In the model, the albedo of the surface is taken to be 0.65 whenever CO_2 frost is present.

A surface slope will change the solar incidence angle and decrease the total thermal emission from the surface. The former is accounted for by calculating the incidence angle separately for the flat and the sloped surfaces, allowing no insolation when the sun is beneath either the flat or sloped horizons. The radiated flux is effectively decreased in rough terrain because some of the emission from the flat surface adjacent to the sloped surface will be absorbed by the latter, and vice versa. To account for this in the model, integrations of the sloped and flat surfaces are performed simultaneously, with each surface absorbing energy emitted by the other. For a slope of angle α, α/π of the flat surfact emission will be incident on the sloped surface and vice versa assuming that each emits uniformly in all directions.

A depth-dependent conductivity is appropriate for the case of a layer of fine material overlying a bedrock surface. To model this, the thermal conductivity is increased discretely at the boundary between two of the model layers.

A surface consisting of areal mixtures of fines and rock, as actually observed at the Viking landing sites, is modeled by summing the radiative fluxes from the individual components. Each component is modelled as an ideal, flat surface of the appropriate thermal inertia in order to obtain the diurnal temperature profile. At each time of day the thermal flux within one of the IRTM passbands is calculated for each component at its respective temperature, and the fluxes are added together weighted by the fraction of the surface covered by each component. The equivalent blackbody temperature is calculated from this net flux. This is the brightness temperature appropriate for a surface composed of patches of the different materials, with each patch larger than the thermal skin depth of the material and much smaller than the field-of-view of the IRTM (5 mrad, or 5 km at a distance of 1000 km). The use of flat patches of rock to obtain the thermal effects of blocks on the surface is an approximation most valid for rocks much larger than the thermal skin depth (about 15 cm) and fair for rocks of that size. A model which explicitly calculated the temperatures of the various faces of a block on the surface was used by Kieffer et al. (1977; Appendix II) to explain the phase angle dependence of the

observed thermal emission, but lacks the smoothness with time desired here.

Surfaces composed of mixes of other materials, such as one with differently-oriented slopes or discrete patches of CO_2 frost, are handled in the same manner as the patches of rock and fines, using the appropriate component temperatures.

Dust present in the atmosphere will decrease the insolation at the surface, retain the thermal emission from the surface, increase the atmospheric temperature, and contribute to the radiances observed by the IRTM. The amount of insolation transmitted, reflected, and absorbed by the dusty atmosphere is calculated with a parameterization by Davies (1979) to a series of Monte Carlo multi-scattering calculations. In the calculations, an empirical scattering function was used to closely match the lander observations. The single-scatter albedo of the dust is taken from the work of Pollack et al. (1979).

The total amount of sunlight absorbed by the dusty atmosphere is obtained by integrating the instantaneous absorption (a function only of indicence angle for given dust opacity and dust scattering properties) over a Martian day. This energy is assumed to be re-radiated equally to space and to the ground at a constant rate throughout the day. The latter assumption is based on a radiative relaxation time of the atmosphere, calculated from the average infrared emissivity of the dust cloud (Martin et al., 1979; Hunt, 1979), which is much longer than a Martian day for a dust visual opacity less than about 1.0.

Some of the infrared surface emission will also be absorbed by the atmospheric dust. To correctly include this term, the absorption of the infrared energy should be integrated over the solid angle of the sky and over all thermal wavelengths. The result will depend strongly, however, on the assumed infrared scattering properties of the dust, which are poorly known. Rather than explicitly including a specific set of dust properties, the amount of infrared energy absorbed is assumed in the model to be equal to the amount of insolation absorbed. This is consistent with the dust model of Hunt (1979). Again, the radiation from the atmosphere to ground is assumed constant with time. The sensitivity to using a different atmospheric radiation term is discussed in the next section.

The thermal radiation emitted by the surface will be modified by emission and absorption within the dusty atmosphere. Thus, the radiance actually observed by the IRTM is moderated by the atmosphere. The atmospheric modification will be strongest at midday and weakest during the night, and will depend on the wavelength band of the observation. Since the determination of thermal inertia from the diurnal temperatures is dominated by the night-time and predawn temperatures, the effect on the derived thermal inertia of seeing through the atmosphere is small and will by ignored.

Not included in any of the models are: sensible heat from the atmosphere; phase changes of water, either in the atmosphere or in the ground; non-Lambertian emission from the surface; transient phenomena of any form, such as carbon dioxide or water clouds; or a temperature dependence of any of the thermal properties. The first and last of these are discussed below.

Sensible heat involves the transfer of energy between the surface and atmosphere as a result of near-surface winds and turbulence. Following Kahle (1977) and Malkus (1962, p. 109), the sensible heat flux into the surface can be represented as

$$H = \rho\, C_p\, C_D\, u_a (T_o - T_a) \qquad (3)$$

where H sensible heat flux

ρ atmospheric density

C_p atmospheric specific heat

C_D drag coefficient of the surface

u_a wind velocity at a height a above the ground

T_o surface temperature

T_a atmospheric temperature at height a

To calculate the magnitude of the heat transfer at the VL-1 landing site as an example, the atmospheric temperature and wind velocity at a height of about 1.6 m are taken from Hess et al. (1976; 1977). Using extreme values of temperature difference and wind velocity, a maximum thermal flux of only about 3% of the maximum solar flux is obtained. This effect is strongest in the mid-afternoon when the solar flux is also strongest and when the surface and atmospheric temperatures differ the most. It is weakest at night, when the temperatures are nearly identical. Thus, sensible heat cannot significantly change the diurnal temperature amplitude, but may produce a small time-dependent deviation from an ideal model. Kieffer et al. (1977, Appendix I) show that the conductive flux in the absence of winds is similarly negligible. On the earth, the atmospheric density is larger such that sensible heat may at times dominate the energy balance (Kahle, 1977),

The variation of surface specific heat, C, with temperature has been noted and applied to the Moon by Winter and Saari (1969). For a surface of very low thermal inertia, with surface temperatures ranging from 130 K to 260 K, C will change by a factor of 2, causing I to change by a factor of 1.4 (e.g., from 1.3 to 1.8). For a surface of intermediate I with temperatures ranging from about 190 K to 290 K, C will change by a factor of 1.4, and I by a factor of 1.2 (e.g., from 6 to 7.2). The diurnal temperatures calculated from the homogeneous model with a constant C, using the extreme-temperature values of C, will bracket the temperatures which would be obtained using a temperature-dependent C. In the first case above, surface temperatures for the two inertias would differ by about 7 K predawn, 5 K in the late morning, 2 K at noon, and almost nothing in the afternoon. In the second case, temperatures differ by less than 4 K both predawn and at noon, and again not at all where the curves cross in the mid-morning and late-afternoon. Therefore, while the thermal inertias determined from the data may differ by a small, calculable amount from the true inertia at some nominal temperature, a variable specific heat will not affect the characteristics of interest in the data (viz., afternoon cooling, morning delay, and spectral contrasts).

A temperature-dependent thermal conductivity K arises from the variability of the solid and radiative components to the conductivity (e.g., Wechsler et al., 1972; see also Fountain and West, 1970). Over the entire temperature range of interest, K will change by

20% at the atmospheric pressures appropriate for the top of the Tharsis volcanoes and only by 8% at the mean surface level. This results in thermal inertia changes of 11% and 4%, respectively. Thus, the variability is smaller than that caused by a temperature-dependent specific heat, and can be ignored.

In the discussion which follows, use is made of several terms related to the derived thermal inertia. The best-fitting model is that ideal (i.e., uniform, flat, and homogeneous) model which most closely reproduces the surface temperatures either as observed or as predicted by one of the non-ideal models. The best-fit is in a least-squares sense, minimizing the difference between the temperatures of the ideal model and those from either the data or the non-ideal model. Generally, the actual data consist of temperatures at several times between local midnight and noon; to match the data, the model which best fits the temperatures of a non-ideal model is determined using temperatures at 24 evenly-spaced times between local midnight and noon. The apparent thermal inertia and albedo of the surface, I_a and A_a, respectively, are the parameters of the best-fitting homogeneous model. The residual between the data or the non-ideal model and the best fitting model temperatures is referred to as $(T - T_{bf})$.

Local Martian times are referred to in units of 1/24 Martian day, each designated as 1 H. Thus, local noon will be 12 H, and dawn occurs at about 6 H. Brightness temperatures in each wavelength band are referred to as T_7, T_9, T_{11}, and T_{20}, as appropriate.

III. RESULTS OF THE MODELS

The apparent thermal inertia I_a of a surface composed of a mixture of different materials will be intermediate between that of the individual components. Fig. 3 shows I_a as would be obtained at 20 μm as a function of the fraction of rock (I = 40) and the fraction of fine material (I = 2) covering the surface. The non-linearity of the curve is due to the non-linearity of both the Planck function and the relationship between thermal inertia and surface temperatures. If all of the variation in thermal inertia on Mars were caused only by varying the fraction of rock coverage at the surface, then the fraction would vary from 0 to about 60%. I_a of this anisothermal surface will vary with wavelength band used since the brightness temperature of the surface varies with wavelength. For a surface half-covered by rock, I_a = 12 observed at 7 μm, while I_a = 9 at 20μm. This model and those shown in Figures 4 through 10 and 12 are calculated specifically for latitude 22° N at areocentric longitude of the sun L_s = 134° (northern summer), but will not very significantly with latitude or season.

If a layer of fine material overlies a rock surface, I will depend on the thickness and thermal inertia of the fine layer (for a discussion of this as applied to the earth, see Watson, 1973). Fig. 4 shows I_a as a function of the thickness of a layer of I = 3 atop rock which has I = 54. The diurnal skin depth of the I = 3 material alone is 2.1 cm, so that a thickness of only one skin depth of fines is sufficient to mask the underlying rock. Reducing the thickness of dust to a half skin-depth increases I_a to about 5. The sub-surface temperature profile of such a surface will be different from that of a homogeneous surface with the same I_a. Most of the daily temperature variation will be confined to the low inertia layer.

In both the layered and patchy-surface models, the residual surface temperature ($T - T_{bf}$) shows an enhanced afternoon cooling similar to that actually observed. The behavior of the patchy surface (Fig. 5) is easily understood as occurring because the diurnal temperature curves for various thermal inertias do not all cross at the same time in the afternoon. Thus, the surface temperature is uniform when the rock and fines temperature curves cross, but is different from the temperature of a material with an intermediate thermal inertia. The behavior of a layered surface (Fig. 6) is not so simple, since the brightness temperature of the surface is not just a combination of the temperatures of the components. Here, the underlying high-inertia rock serves to moderate the noon and predawn temperatures, while the low-inertia dust dominates at sunrise and sunset, when the most sudden changes in insolation occur. Because the best-fitting model is determined from morning temperatures, the morning residuals are smaller than the afternoon ones; the result is the large afternoon cooling shown in Fig. 6. Both the layered and patchy models predict a morning rise in temperature of about 5K relative to a homogeneous surface. The data can generally neither confirm nor refute this difference due to the low temporal resolution.

The degree of afternoon cooling derived from the patchy model will depend on the fraction of surface covered by fine material. There will be no effect when the surface consists entirely of one component. The maximum afternoon cooling of about 12 K occurs with about 50% rock coverage ($I_a = 9$). If the fines have an inertia higher than $I = 2$, then an I_a of 9 will require less rock coverage and the afternoon cooling obtained will be appropriately smaller. Similarly, a

layered surface will show no afternoon cooling for either a zero or a large thickness of overlying dust, and up to about 30 K for an intermediate thickness.

Since a surface which is anisothermal on a scale smaller than the IRTM resolution will have a brightness temperature which decreases with wavelength due to the non-linearity of the Planck function, observations of a patchy surface are expected to show this behavior. The solid line of Fig. 7 shows the predawn difference between T_7 and T_{20} expected for a surface composed of various fractions of rock (I = 40) and fines (I = 2). The points represent data taken from the Syria Planum and Tharsis regions on Mars. That the curve and data are so dissimilar in nature indicated that the major contribution to at least the predawn spectral temperature differences arises from some mechanism other than surface anisothermalities, possibly atmospheric effects (See Martin et al., 1979; and Hunt, 1979). However, notice that temperature differences of up to 14 K can result from surface anisothermalities, and results that depend on the spectral contrasts, such as the atmospheric opacity (Martin et al., 1979) or atmospheric structure and cloud composition (Hunt, 1979) may be biased.

A sloping surface will exhibit surface temperatures throughout the day different from those of a flat surface. A west-facing slope will absorb less of the early-morning sun and the surface temperatures will increase slower at dawn than those of a flat surface, causing the surface to appear (based on the morning temperatures) as one of higher inertia. Likewise, an east-facing slope will exhibit an enhanced response to the sun and will appear to be of lower

I than a west-facing slope. For small slopes ($\leq 10^{o}$), the apparent thermal inertia of the sloped surface alone varies nearly linearly with the slope angle. I_a is shown as a function of the azimuth of the slope for a slope of 8^{o} in Fig. 8. Notice that the total range of I_a is only about 1. over all azimuths.

An undulating surface with slopes distributed randomly in all directions is modeled as consisting of a mix of many sloped surface elements, each with the same slope angle, but oriented at different azimuths. The resulting I_a is almost unchanged from the actual inertia of the material. For instance, for surfaces of I = 6.5 at the large average slope of 10^{o}, I_a = 7.0. For the relatively small slopes considered here, the surface anisothermality is not great enough to produce spectral temperature differences of more than about 1 K.

The thermal effects of various other surface structures, such as sand dunes, craters, volcanoes, mountains, or channels, could be modelled by accumulating the effects due to slopes. This is not shown here as no systematic comparison with the data has been performed.

The visual optical thickness of the dust in the atmosphere was measured from the landing sites to be about 0.5 prior to the onset of the dust storms (Pollack et al., 1977, 1979). These measurements must be taken as a maximum value since the observations were limited to the early morning and late afternoon, when local fogs or clouds may have been present. The opacity was also determined from orbiter images (Thorpe, 1977) assuming a lunar-like surface photometric function, with the values typically being about 0.1-0.2. I_a for a surface beneath a dusty atmosphere is shown in

Fig. 9 for various actual thermal inertias. Recall that this ignores the effects of seeing through the atmosphere from above (see section II).. The curve for I = 0 is for a surface which is in thermal equilibrium with the atmosphere at night and with the sun and atmosphere during the day. As opacity increases, the atmospheric contribution increases, so that the I = 0 surface has a decreasing diurnal amplitude and thus appears to have a non-zero thermal inertia. This means that with an opacity $\tau = 0.3$, for instance, no real surface could have $I_a \leq 3$. Under the same dusty atmosphere, a surface with I = 6 will have $I_a = 9.3$. Calculations done for different amounts of atmospheric radiation to the surface at the same visual opacity, to determine the effects of various dust scattering properties, show that the change in I_a is approximately linear with the amount of atmospheric radiation. Thus, if only 80% as much surface thermal emission is absorbed by the atmosphere as is assumed in these models, the I = 6 surface, with $\tau = 0.3$, would have I_a 9.0 instead of 9.3.

A dusty atmosphere will also produce an enhanced afternoon cooling of the surface relative to the homogeneous models, with very little effect immediately after sunrise. Fig. 10 shows the temperature difference $(T - T_{bf})$ for a homogeneous surface beneath a dusty atmosphere. An I = 4 surface, with $\tau = 0.3$, will have $I_a = 7$ and an afternoon cooling of about 10 K.

IV. DISCUSSION

The models discussed in the previous sections can be applied to specific local and global areas of Mars, with some interesting results.

The Viking-1 landing site is one place the models can be applied, assuming that the region surrounding the site to a distance of several kilometers (the IRTM field of view) is similar to the immediate surroundings of the lander. The landing site consists essentially of a fine material with intermixed rocks covering about 8% of the surface area (R. Arvidson, personal communication to Kieffer, 1976). The apparent thermal inertia of the area is 9 ± 0.5 (Kieffer et al., 1976a; Kieffer, 1976). If only the surface rocks and fine material contribute to I_a, then the thermal inertia of the fine component must be about 8. This corresponds to an average particle size for the fine material of about 0.05 cm. The actual size of the fine material is less than this (Shorthill et al., 1976), and an inertia of 4 (average particle size of ~100μm) might be more appropriate. To resolve this discrepancy, Kieffer (1976) postulated a bonding of the material, resulting in a larger conductivity than expected for that size of particles and hence a larger I_a. In fact, such a surface bonding into a "duri-crust" is observed at the VL-1 site (Shorthill et al., 1976). The effect of this bonding on the conductivity of the material is not known; however, a factor of four increase is required to account for the high inertia of the fine material.

If the effects of the dust in the atmosphere are included, the actual surface thermal inertia will be lower than the apparent value

I_a = 9. From Fig 9, if the opacity τ = 0.3, (see previous section) the actual inertia is seen to be about 6. Removing the effects of the rocks leads to a value of about 5 for the inertia of the fine material. This corresponds to an average particle size of about 160μm, which is closer to the range of particle sizes determined from the lander, and requires a much smaller increase in thermal conductivity from bonding of the fine meterial.

It is of interest to construct a complete thermal model for the VL-1 site, with the surface consisting of 8% rock (I = 40) and 92% fines (I = 5, see above), and an atmospheric opacity τ = 0.3. Of course the apparent thermal inertia of this surface is I_a = 9. Additionally, the non-ideal model predicts an afternoon cooling at 20μm of up to about 9 K relative to the best-fitting homogeneous model. The observed T_{20} values also show an afternoon cooling of up to 8 K, suggesting that the combination of mixing of materials and the presence of dust in the atmosphere may be responsible for this effect.

An interesting result is found if we examine the data taken entirely within the caldera of Arsia Mons volcano. The elevation there is about 27 km above the Martian mean, and the largest fraction of any atmospheric dust is probably below this level, especially during the relatively clear primary mission. Also, as will be seen, the apparent inertia is low enough that not enough rock can be mixed in to cause the observed afternoon cooling.

The caldera appears in images as a relatively smooth, flat, featureless region, with no large-scale surface roughness (Carr et al., 1977). Any deviations of the temperatures from those expected for a homogeneous, flat surface or mixture of materials could plausibly be due to small-scale roughness.

The observed brightness temperatures (T_{20}) within the caldera are shown in Fig. 11. The apparent inertia, obtained by fitting homogeneous models to the data, is about 1.2. However, at the elevation of Arsia Mons, the atmospheric radiation to the surface is much smaller than the 0.02 of the noontime solar flux assumed in the homogeneous model, so a fit was done using models which included no atmospheric radiation term. This resulted in $I_a = 2.0$.

The Arsia Mons data show both a morning delay and an afternoon cooling relative to the best-fitting model. The former suggests a surface partially covered with CO_2 frost, such that just after sunrise the uncovered portion responds to the insolation while the frost covered part remains at the frost-point temperature (Kieffer et al., 1976b). The diurnal temperature curves for such a model are also shown in Fig.11 . To create a delay with a uniform surface requires an inertia low enough to allow frost formation at night, but then there is no post-dawn rise in temperature until all the frost has sublimed. A mixed surface, however, will have a gradual post-dawn temperature increase followed by a steeper rise upon sublimation of all the CO_2 frost. The mixed surface model shown in Fig. 11, consisting of 80% I = 1.2 (with

frost formation at night) and 20% I = 4.0 (no frost), adequately describes all of the morning data.

For this mixed surface, one would expect anisothermally-induced spectral differences between the channels. The observed temperature difference $T_{10}-T_{20}$, which will be positive as a result of anisothermalities on the surface, is about 6K at 6.5H (just after sunrise), rises to about 12K at 7.5H, and drops to near zero at 9H, consistent with what is expected.

The afternoon temperatures, however, are about 25K cooler than those expected from the mixed surface model. The two components are both of such a low inertia that there is little predicted afternoon cooling due to the surface mixing. One possible explanation is that the afternoon observations are biased, such that the cooler, shaded sides of any surface roughness features were observed. The thermal inertia of the material is low enough that even small-scale features (e.g., 10 cm across) can produce this effect. The phase angle of the observations is about 110°, so that the shadowed regions are in fact preferentially observed.

Finally, several interesting features show up in the global correlation of thermal inertia with surface elevation. Fig. 12 shows a histogram of I_a versus elevation. The thermal inertias are those mapped by Kieffer et al. (1977) on a 2° latitude by 2° longitude bin size, and cover most of the region from -30° to +10° latitude. The elevations are from the published topographic map of Mars (USGS, 1976). The most striking correlation in the

histogram (Fig. 12) is the trend from intermediate inertias ($I_a \approx 9$) at low elevations to low inertias ($I_a \approx 3$) at high elevations. In addition to this is a grouping of low inertias at low elevations ($I_a \approx 2$-3, elevations around 0 km), and another grouping at intermediate values of both the elevation and inertia ($I_a \approx 5$-8, elevations between 6 and 9 km). While not included in the histogram, the thermal inertias in the Elysium region (Peterfreund et al., 1977) and those determined from the northern hemisphere nighttime temperatures of Zimbelman and Kieffer (1979) are generally consistent with the trends shown.

There are several possible causes for a correlation between I_a and elevation. The thermal conductivity, and hence the thermal inertia, of a porous material will depend on the pressure of the inter-particle gas (Wechsler et al., 1972; Wechsler and Glasar, 1965), with a higher pressure increasing the thermal inertia. The thermal inertia of a powdered material varies apporiximately as the fourth root of pressure for relevant pressures (Kieffer et al., 1973), such that going from the summit of the large volcanoes to the mean surface lavel will increase the thermal inertia of a porous material by a factor of about 1.8 (e.g., an inertia of 2.0 on top of Arsia Mons becomes 3.6 at lower elevations).

Dust distributed within the atmosphere will cause a change in the apparent inertia with elevation. As seen before, increasing the amount of dust in the atmosphere increases I_a. Thus, at higher elevations, where the opacity of the atmosphere is lower, I_a should also be lower. Assuming that the dust has the same scale height as the gas in the atmosphere (about 10 km) the opacity at the volcano summits will be only 0.06 that at the elevation of the VL-1 lander.

The contribution of the thermal radiation from the atmosphere to the surface will vary with elevation due to the decrease in absorption of thermal energy by CO_2 at higher elevations. Thus, the inertias calculated assuming an atmospheric radiation term appropriate for low elevation will be too low. As discussed earlier, the caldera of Arsia Mons has $I_a = 1.2$ calculated from the standard models, but $I_a = 2.0$ from models with no radiative contribution from the atmosphere.

Lastly, a correlation between elevation and apparent thermal inertia may be caused by a real change in the particle size distribution with elevation (see Zimbelman and Kieffer, 1979). For instance, wind-blown dust may be deposited preferentially with finer material at higher elevations.

All of the mechanisms mentioned above, act to produce lower apparent inertias at higher elevations. That all of the data does not lie along a single line trending toward low inertias at high elevations indicates that the above-mentioned processes alone have not acted uniformly over the entire planet. The relationships between elevation and apparent inertia predicted by some of the mechanisms are also shown in Fig. 12. The solid line shows the thermal inertia changes expected solely from the pressure changes with elevation, for an inertia of 8.3 at -1.5 km elevation. At 10 km, the resulting inertia is 6.4, and at 27 km it is 4.2. The dotted line includes also the changing atmospheric radiation to the surface and results in $I_a = 5.7$ at 10 km and 3.5 at 27 km. The dashed line takes into account the dust in the atmosphere, showing the apparent thermal inertia for that surface with would yield $I_a = 8.3$ at -1.5 km. Thus, assuming $\tau = 0.3$ at -1.5, $I_a = 4.1$ at 10 km and 1.9 at 27 km. Recall that the actual variation of apparent inertia with dust

opacity depends on the assumptions of dust properties, and that this curve may be displaced in either direction by an inertia of less than 0.5 at higher elevations. It is the dotted line that the data would be expected to follow if the atmosphere were free of dust and if the surface physical properties were constant with location and only the elevation changed; the data would follow the dashed line if there were sufficient dust in the atmosphere to yield $\tau = 0.3$ at -1.5 km. Less dust in the atmosphere will cause the dashed line to shift toward higher inertias, while more dust will shift it toward lower inertias.

It is apparent that the surface properties are not as stratified with elevation as originally thought by Kieffer et al. (1976b), and that the regions at higher elevations upon the Tharsis plateau are not so dissimilar from the lower-elevation regions, for instance the Viking landing sites. The difference could be explained almost entirely by the absence at the higher elevations of the exposed rock present at the landing site or, equivalently, by the covering up of the exposed surfaces at high elevations by windblown dust.

However, even at the higher elevations, the thermal inertia histogram appears bimodal, for instance with peaks at inertias of 3.5 and 6.0 at 9.0 km elevation. The lower inertia values correspond to the regions immediately surrounding the Tharsis volcanoes, including the Noctis Labyrinthus region at the western end of the Valles Marineris. The higher-inertia values are provided by the Syria Planum area to the south. At the lower elevation of 7 km, the areas to the northwest contribute to the lower inertias, while those to the southeast contribute to the higher inertias. Thus, the Tharsis volcano region may be similar in physical composition to other, intermediate-inertia, regions at lower elevations, such as Sinus Meridiani or

Syrtis Major Planitia. The VL-1 site, in a region described as cratered plains by Scott and Carr (1978), appears to be somewhat similar to the higher-inertia material at high elevations, also mapped as cratered plains.

The grouping at low inertias and low elevations includes the Amazonis Planitia area, to the west of Olympus Mons, and extends about 30° in longitude further west. The apparent thermal inertias here are so low that subtracting out the effects of airborne dust results in inertias of about 1, corresponding to an average particle size of less than 50μm (Kieffer et al., 1973). Distinction cannot easily be made, however, between this and a surface with an actual inertia of about 2.5 beneath a locally dust-free atmosphere.

It should be apparent at this point that the variation of thermal inertia with location on Mars cannot be explained by the variation of a single property, be it elevation, fraction of rock covering the surface, or particle size of the fine material. The global bimodal distribution of thermal inertia , with peaks at inertias of about 2.5 and 6., has been interpreted as an association between areas of aeolian erosion and the higher inertias, and between areas of aeolian deposition and the lower inertias (Kieffer et al., 1977), or as a distinction between materials derived from different mineralogic or chemical source regions (Kieffer and Palluconi, 1978). An alternative explanation, suggested by Horai (1979), is that the low-inertia peak in the distribution is simply due to the presence of a loosely-packed soil, while the high-inertia peak results from a compacted soil. From the histogram in Fig. 12, it is apparent

that while the inertias are distributed into at least two distinct classes, the thermal inertia alone is not the determining factor. Rather, the first group consists of the area near Amazonis, with low inertias at low elevations, and the second consists of the remaining regions. The latter group can again be subdivided, although the genetic relationships between and within the groups are not at all clear.

While the discussion by Horai (1979) is somewhat oversimplified, the data supports his basic premise, that the Martian surface consists of at least two distinct units, one of low inertia ($I < 3$) and one of intermediate inertia ($I \approx 6$). That these units are not without variations is seen in the histogram and by the variation of the inertia of the fine material between the two Viking landing sites, being 8. and 6.2 at the VL-1 and VL-2 sites, respectively (ignoring effects of the dust). Thus, the variation in thermal inertia over the planet is seen to be caused by : 1) the variation in surface elevation, with its effects due to the changing pressure and dust opacity; 2) changes in the fraction of exposed rock covering the surface; and 3) changes in the thermal inertia of the fine material.

V. SUMMARY

The variation in the thermal inertia with location on Mars is determined by the variation of the surface and atmospheric properties which affect the surface temperatures. These include rock exposed at the surface, surface particle size distribution, surface slopes, CO_2 condensed onto the surface, any fine material overlying rock, dust in the atmosphere, and transient phenomena, including clouds, fog, and sensible heat from surface winds. The former properties have been modeled to determine explicitly their effects on the derived thermal inertias.

The model results were then applied to the data covering various regions. The temperatures observed at the VL-1 landing site, along with the cooling in the afternoon relative to any reasonable homogeneous surface models, were adequately reproduced by the non-ideal model which included observed amounts of surface rocks and atmospheric dust. The morning data from the large caldera of Arsia Mons were fit by a model which included a mixing of surface materials. However, the large afternoon cooling effect there was not reproduced, probably as a result of the large phase angle of the observations.

The histogram of apparent thermal inertia versus surface elevation shows at least two classes of material, different from the two classes discussed by Kieffer et al. (1977). One, at low elevations, is of a low thermal inertia and hence very fine. The other extends from high inertias at low elevations to lower inertias at high elevations. much of this latter variation can be explained by the changing elevation,

with the material properties remaining constant with location. The rest of the latter variation is presumably due to changes in the average particle size of the surface.

ACKNOWLEDGMENTS

I am indebted to many people for their useful discussions and advice, including P.R. Christensen, A.R. Gillespie, H.H. Kieffer, T.Z. Martin, R. Mehlman, E.D. Miner, D.O. Muhleman, F.D. Palluconi, and A.R. Peterfreund. I thank H.H. Kieffer for allowing me to use and modify his surface thermal model computer program. L. Wainio digitized the topographic map of Mars. I am grateful for comments received on an earlier version of this manuscript to H.H. Kieffer, A.R. Gillespie, D.O. Muhleman, and F.D. Palluconi. K. Campbell and C. Seale typed the manuscript. Some of this work was done while at the University of California at Los Angeles, under NASA contract 952988. Partial support was received at Caltech under NASA grants NGL 05-002-003 and NSG 7565.

REFERENCES

Carr, M.H., R. Greeley, K.R. Blasius, J.E. Guest, and J.B. Murray, Some Martian Volcanic Features as Viewed From the Viking Orbiters, J. Geophys. Res., 82, 3985-4015, 1977.

Carslaw, H.S. and J.C. Jaeger, Conduction of Heat in Solids, 2nd edition, Oxford University Press, London, 1959.

Chase, S.C., Jr., J.L. Engel, H.W. Eyerly, H.H. Kieffer, F.D. Palluconi, and D. Schofield, Viking Infrared Thermal Mapper, App. Optics, 17, 1243-1251, 1978.

Chase, S.C., E.D. Miner, D. Morrison, G. Münch, and G. Neugebauer, Mariner 10 Infrared Radiometer Results: Temperatures and Thermal Properties of the Surface of Mercury, Icarus, 28, 565-578, 1976.

Davies, D.W., Effects of Dust on the Heating of Mars' Surface and Atmosphere, submitted to J. Geophys. Res., 1979.

Fountain, J.A. and E.A. West, Thermal Conductivity of Particulate Basalt as a Function of Density in Simulated Lunar and Martian Environments, J. Geophys. Res., 75, 4063-4069, 1970.

Gillespie, A.R. and A.B. Kahle, Construction and Interpretation of a Digital Thermal Inertia Image, Photogramm. Eng. and Remote Sensing, 43, 983-1000, 1977.

Hess, S.L., R.M. Henry, C.B. Leovy, J.A. Ryan, and J.E. Tillman, Meteorological Results From the Surface of Mars: Viking 1 and 2, J. Geophys. Res., 82, 4559-4574, 1977.

Hess, S.L., R.M. Henry, C.B. Leovy, J.A. Ryan, J.E. Tillman, T.E. Chamberlain, H.L. Cole, R.G. Dutton, G.C. Greene, W.E. Simon, and J.L. Mitchell, Preliminary Meteorological Results on Mars from the Viking 1 Lander, Science, 193, 788-791, 1976.

Horai, K.-I., Loose and Compacted Soils: Two Basic Units Composing the Martian Surface? (abstract), in Lunar and Planetary Science X, The Lunar and Planetary Science Institute, Houston, 564-566, 1979.

Hunt, G.E., Thermal Infrared Properties of the Martian Atmosphere. IV. On Predictions of the Structure of Martian Atmosphere in the Presence of Dust Storms and Ice Clouds from the Viking IRTM Spectral Measurements, J. Geophys. Res., in press, 1979.

Hunt, G.R. and R.K. Vincent, The Behavior of Spectral Features in the Infrared Emission from Particulate Surfaces of Various Grain Sizes, J. Geophys. Res., 73, 6039-6046, 1968.

Ingrao, H.C., A.T. Young, and J.L. Linsky, A Critical Analysis of Lunar Temperature Measurements in the Infrared, in The Nature of the Lunar Surface (W.N. Hess, D.H. Menzel, and J.A. O'Keefe, eds.), John Hopkins Press, Baltimore, Md., 185-211, 1966.

Jaeger, J.C., Conduction of Heat in a Solid with Periodic Boundary Conditions, with an Application to the Surface Temperature of the Moon, Proc. Cambridge Phil. Soc., 49, 335-359, 1953.

Jones, K.L., R.E. Arvidson, E.A. Guinness, S.L. Bragg, S.D. Wall C.E. Carlston, and D.G. Pidek, One Mars Year: Viking Lander Imaging Observations, Science, 204, 799-806, 1979.

Kahle, A.B., A Simple Thermal Model of the Earth's Surface for Geologic Mapping by Remote Sensing, J. Geophys. Res., 82, 1673-1680, 1977.

Kieffer, H.H., Soil and Surface Temperatures at the Viking Landing Sites, Science, 194, 1344-1346, 1976.

Kieffer, H.H., S.C. Chase, E.D. Miner, G. Münch, and G. Neugebauer, Preliminary Report on Infrared Radiometric Measurements from the Mariner 9 Spacecraft, J. Geophys. Res., 78, 4291-4312, 1973.

Kieffer, H.H., S.C. Chase, Jr., E.D. Miner, F.D. Palluconi, G. Münch, G. Neugebauer, and T.Z. Martin, Infrared Thermal Mapping of the Martian Surface and Atmosphere: First Results, Science, 193, 780-786, 1976a.

Kieffer, H.H., P.R. Christensen, T.Z. Martin, E.D. Miner, and F.D. Palluconi, Temperatures of the Martian Surfaces and Atmosphere: Viking Observations of Diurnal and Geometric Variations, Science, 194, 1346-1351, 1976b.

Kieffer, H.H., T.Z. Martin, A.R. Peterfreund, B.M. Jakosky, E.D. Miner, and F.D. Palluconi, Thermal and Albedo Mapping of Mars During the Viking Primary Mission, J. Geophys. Res., 82, 4249-4291, 1977.

Kieffer, H.H. and F.D. Palluconi, Martian Surface Particle Size Determined by Thermal Mapping (abstract), in NASA TM-78,455, 27-29, 1978.

Malkus, J.S., Large-Scale Interactions, in The Sea, vol. 1 (M.N. Hill, ed.), Wiley and Sons, N.Y., 88-322, 1962.

Martin, T.Z., A.R. Peterfreund, E.D. Miner, H.H. Kieffer, and G.E. Hunt, Thermal Infrared Properties of the Martian Atmosphere. I. Global Behavior at 7, 9, 11, and 20 μm, J. Geophys. Res., in press, 1979.

Mutch, T.A., A.B. Binder, F.O. Huck, E.C. Levinthal, S. Liebes, Jr., E.C. Morris, W.R. Patterson, J.B. Pollack, C. Sagan, and G.R. Taylor, The Surface of Mars: The View from the Viking 1 Lander, Science, 193, 791-801, 1976.

Peterfreund, A.R., H.H. Kieffer, and F.D. Palluconi, Thermal Inertia of the Elysium Region of Mares (abstract), in Lunar Science XIII, p. 765-768, The Lunar Science Institute, Houston, 1977.

Pollack, J.B., D.S. Colburn, F.M. Flasar, C.E. Carlston, and D. Pittock, Properties and Effects of Dust Particles Suspended in the Martian Atmosphere, J. Geophys. Res., in press, 1979.

Pollack, J.B., D. Colburn, R. Kahn, J. Hunter, W. Van Camp, C.E. Carlston, and M.R. Wolf, Properties of Aerosols in the Martian Atmosphere, as Inferred From Viking Lander Imaging Data, J. Geophys. Res., 82, 4479-4496, 1977.

Scott, D.H. and M.H. Carr, Geologic Map of Mars, Map I-1083, U.S. Geological Survey, Washington, D.C., 1978.

Shorthill, R.W., H.J. Moore II, R.E. Hutton, R.F. Scott, and C.R. Spitzer, The Environs of Viking 2 Lander, Science, 194, 1309-1318, 1976.

Thorpe, T.E., Viking Orbiter Observations of Atmospheric Opacity During July-November 1976, J. Geophys. Res., 82, 4151-4159, 1977.

U.S. Geological Survey, Topographic Map of Mars, Map I-961, U.S. Geological Survey, Washington, D.C., 1976.

Watson, K., Periodic Heating of a Layer Over a Semi-Infinite Solid, J. Geophy. Res., 78, 5904-5910, 1973.

Wechsler, A.E. and P.E. Glaser, Pressure Effects on Postulated Lunar Materials, Icarus, 4, 335-352, 1965.

Wechsler, A.E., P.E. Glaser, and J.A. Fountain, Thermal Properties of Granulated Materials, in Thermal Characteristics of the Moon (J.W. Lucas, ed.), M.I.T. Press, Cambridge, Mass., 215-241, 1972.

Winter, D.F. and J.M. Saari, A Particulate Thermophysical Model of the Lunar Surface, Astrophys. J., 156, 1135-1151, 1969.

Zimbelman, J.R. and H.H. Kieffer, Thermal Mapping of the Northern Equatorial and Temperate Latitudes of Mars, J. Geophys. Res., this issue, 1979.

FIGURE CAPTIONS

1. An extreme example of the enhanced afternoon cooling, where the afternoon temperatures are about 21 K lower than those expected from the homogeneous model which best fits the morning data. The data is from just off the west flanks of Pavonis Mons volcano, taken on VO-1 revs 90 and 91. The apparent inertia and albedo are $I_a = 2.8$ and $A_a = 0.26$.

2. The observed diurnal variation in the difference between T_7 and T_9 for two latitude bands and seven time periods. $L_s = 120°$ is early in the Viking primary mission and corresponds to late northern summer. From Martin et al. (1979).

3. The apparent thermal inertia of a surface composed of various fractions of surfaces with I = 2 and I = 40, respectively, as would be obtained using observed values of T_{20}. The curves for the other IRTM spectral bands will lie above this one, due to the non-linearity of the Planck function.

4. The apparent thermal inertia of a surface consisting of fine material with I = 3 atop rock with I = 54 as a function of the thickness of the fine layer. The diurnal thermal skin depth of the fines alone is 2.1 cm. The apparent upturn in inertia as the fine layer thickens is an artifact of the digitization of the calculations.

5. The residual temperature ($T - T_{hf}$) between the surface temperatures predicted for the patchy surface model (see Fig.3)and the temperatures of the best-fitting homogeneous model, fit to the morning temperatures. This shows the enhanced afternoon cooling effect for three values of the fraction of the surface covered by fine material. The apparent thermal inertias of the three surfaces are 4, 9, and 21, respectively.

6. Same as Fig. 5, but for a surface composed of a layer of fines lying on top of rock. The solid line is for 0.25 cm of fine material (I = 3), and the dashed line is for 1.30 cm. The surfaces have apparent thermal inertias of about 12 and 4, respectively.

7. Predawn difference between T_7 and T_{20} versus the apparent thermal inertia of the surface. The solid line shows the expected spectral differences as a function of I_a for an otherwise uniform surface composed of patches of materials with I = 2 and I = 40 . The dots show the actual data for a region including the Tharsis volcanoes and Syria Planum taken on VO-1 revs 60 and 62 during the primary mission. The disagreement between the model and the data suggests that another mechanism is operating here, probably the result of early-morning clouds or fogs (see Martin et al., 1979).

8. The apparent inertia of an 8° sloped surface with I = 6.5 as a function of the azimuth of the slope.

9. The apparent thermal inertia of a surface as a function of the visual optical thickness . of the dust in the atmosphere. The lines are shown for various clear-atmosphere thermal inertias. The zero inertia line is for a surface in radiative equilibrium with the sun and atmosphere. See text for details.

10. Residual temperature ($T - T_{bf}$) for an I = 4 surface beneath a dusty atmosphere, with $\tau = 0.1$ (dashed line) and $\tau = 0.3$ (solid line).

11. Temperatures and models for the caldera of Arsia Mons. The data is from VO-1 revs 51 to 64 and VO-2 rev 15, at about $L_s = 110°$ (northern summer). The model curves labeled I = 1.2 and I = 4 are the temperatures of the homogeneous surface with those thermal inertias. The model labeled mix is for a surface consisting of 20% I = 4 and 80% I = 1.2

12. Histogram of thermal inertia vs. surface elevation. N_{max} is the number of data points in the tallest bin at that elevation. The Viking landing sites are shown as a circle (VL-1) and a cross (VL-2). The solid line shows the relationship expected solely from the change in thermal conductivity due to the changing surface pressure with elevation. The dotted line includes also the effect of the changing atmospheric radiation term with elevation due to the variation of atmospheric airmass. The dashed line includes the effects of atmospheric dust on the apparent thermal inertia given a dust opacity $\tau = 0.3$ at -1.5 km elevation. The arrows mark the thermal inertias of the three models at an elevation of 27 km.

Fig. 1

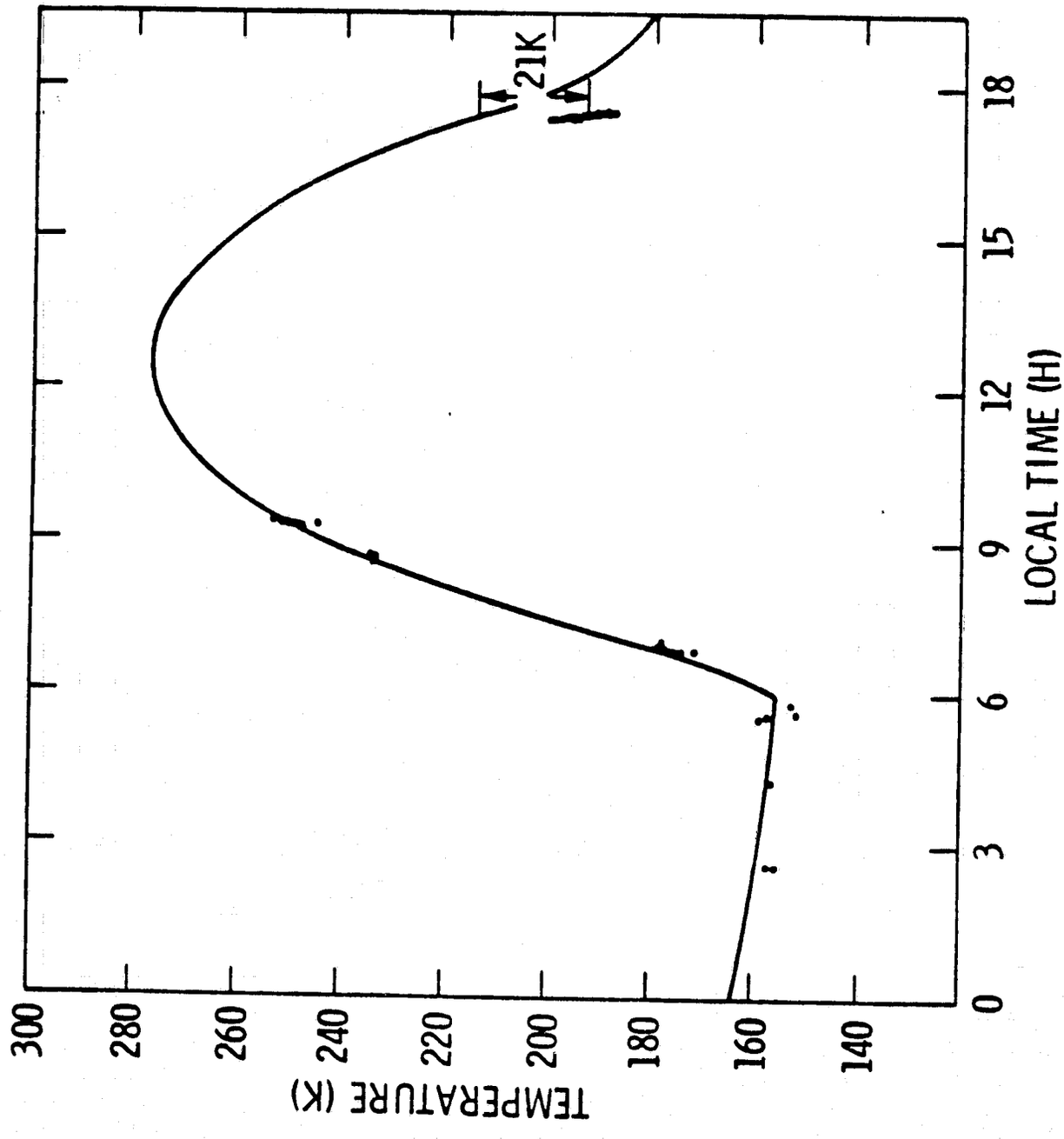
T_{21K}
TEMPERATURE (K)
300
280
260
240
220
200
180
160
140
0
3
6
9
12
15
18
LOCAL TIME (H)

Fig. 2

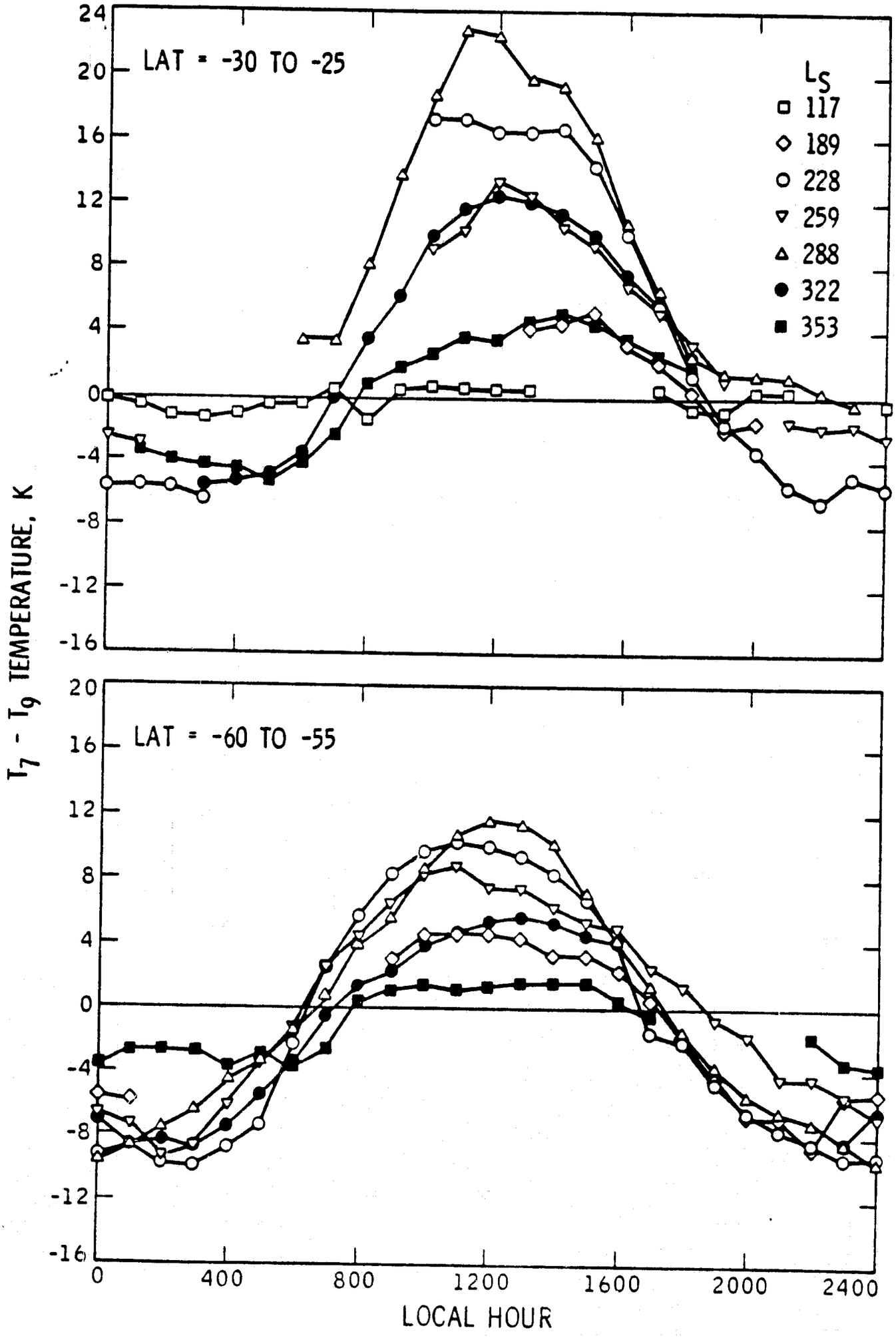
LAT = -30 TO -25
LAT = -60 TO -55
L_S
117
189
228
259
288
322
353
$T_7 - T_9$ TEMPERATURE, K
LOCAL HOUR
24
20
16
12
8
4
0
-4
-8
-12
-16
0
400
800
1200
1600
2000
2400

Fig. 3

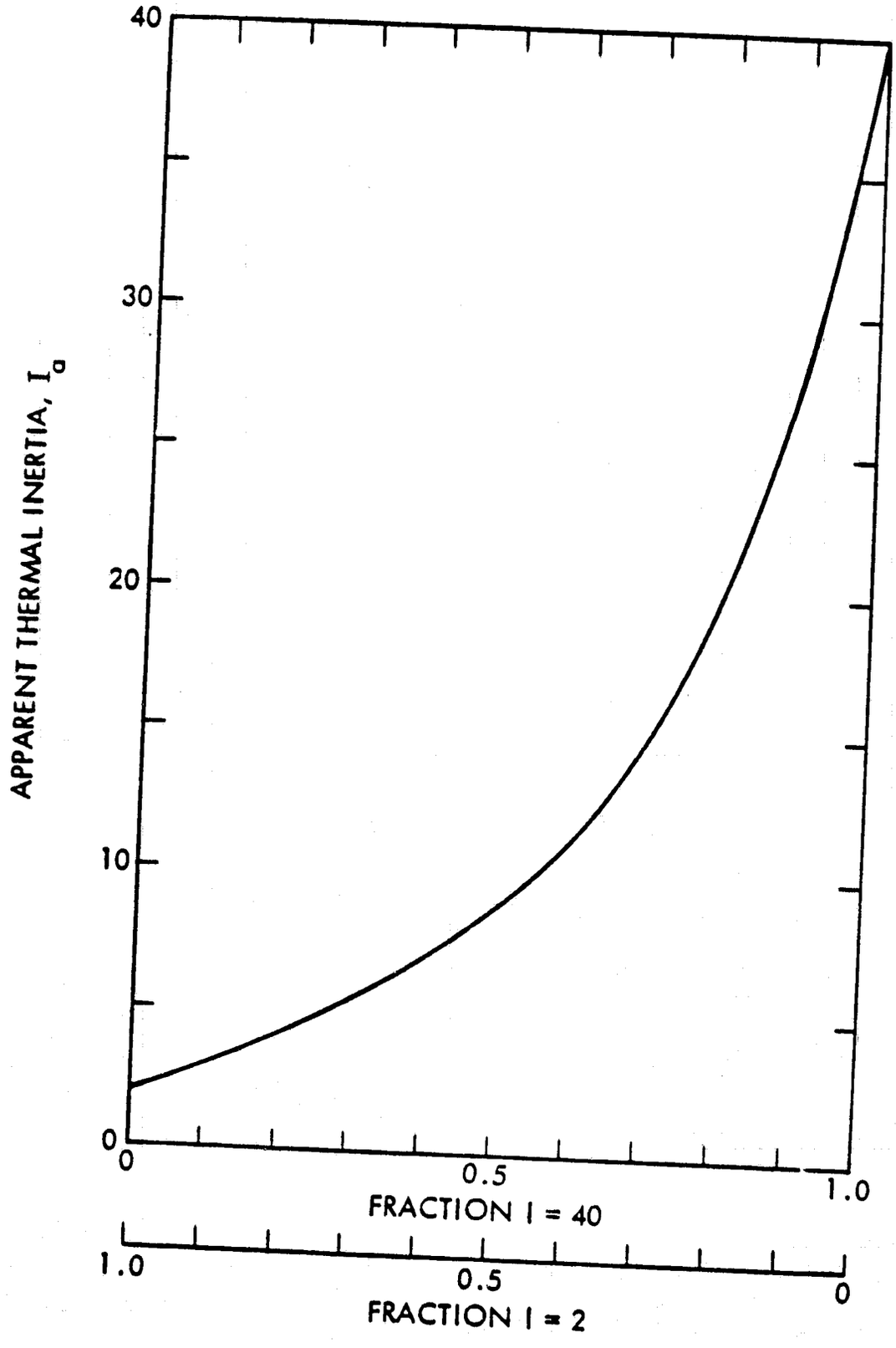
APPARENT THERMAL INERTIA, I_a
40
30
20
10
0
0
0.5
1.0
FRACTION I = 40
1.0
0.5
0
FRACTION I = 2

Fig. 4

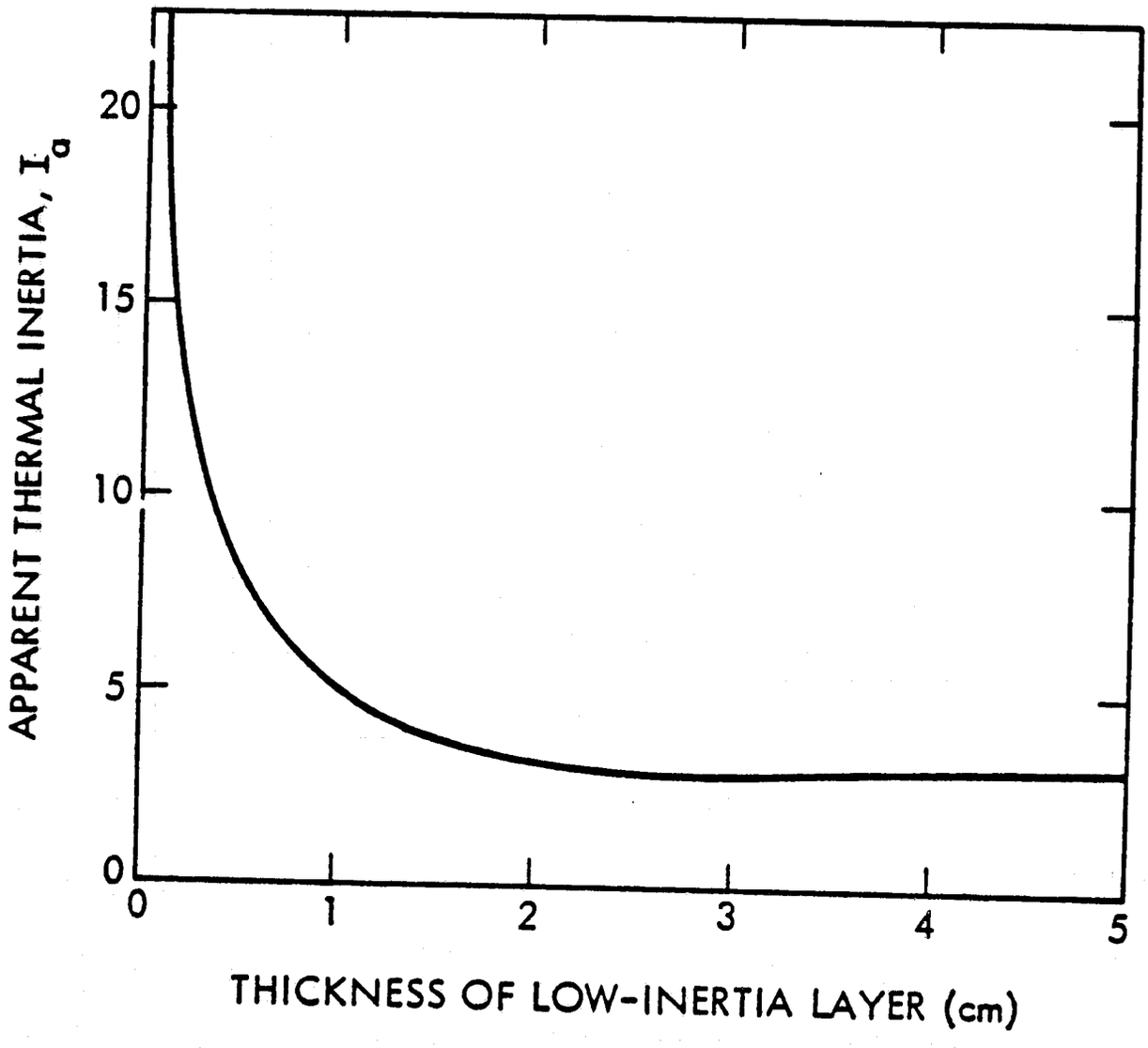
APPARENT THERMAL INERTIA, I_a
20
15
10
5
0
0
1
2
3
4
5
THICKNESS OF LOW-INERTIA LAYER (cm)

Fig. 5

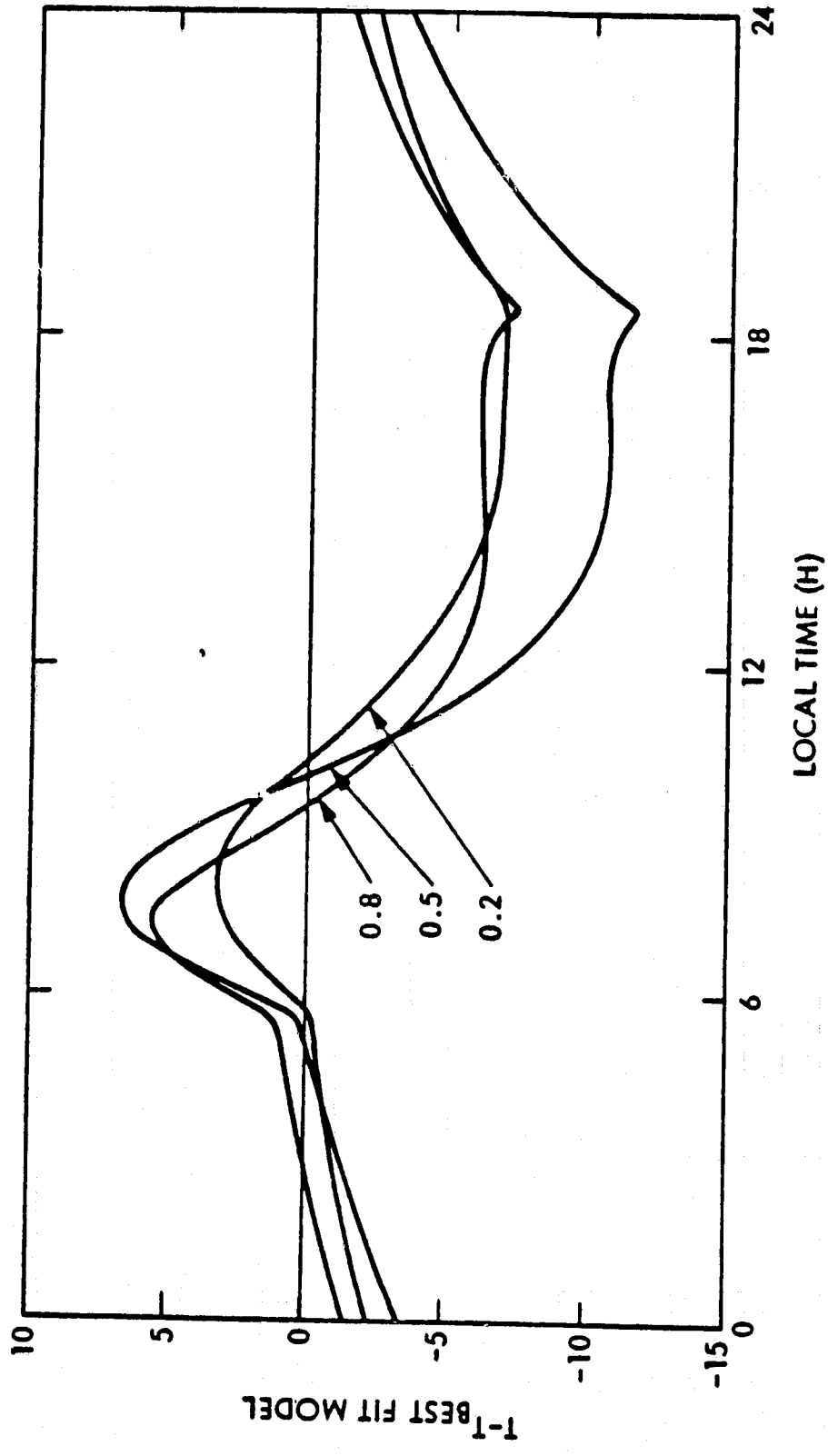

Fig. 6

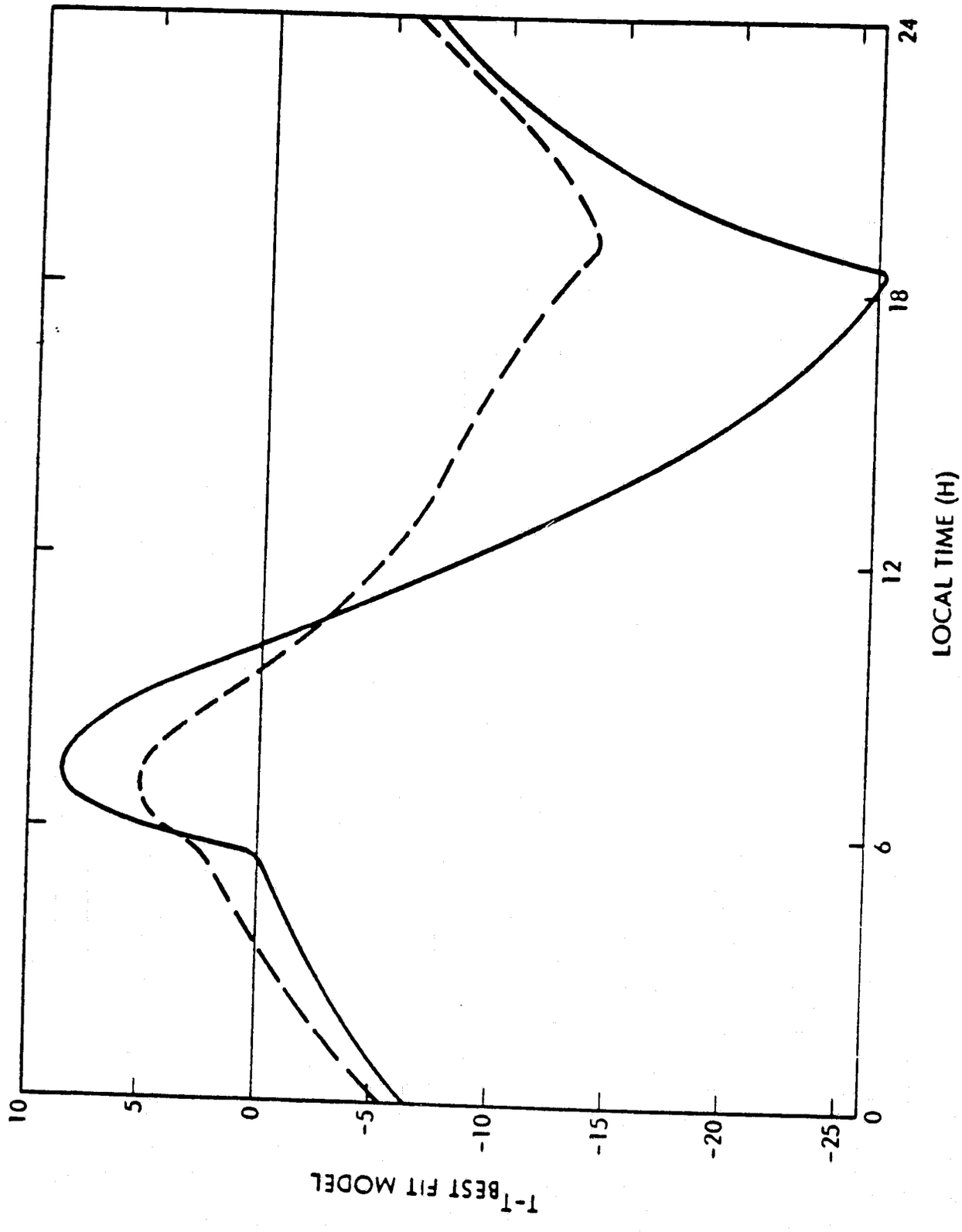

Fig. 7

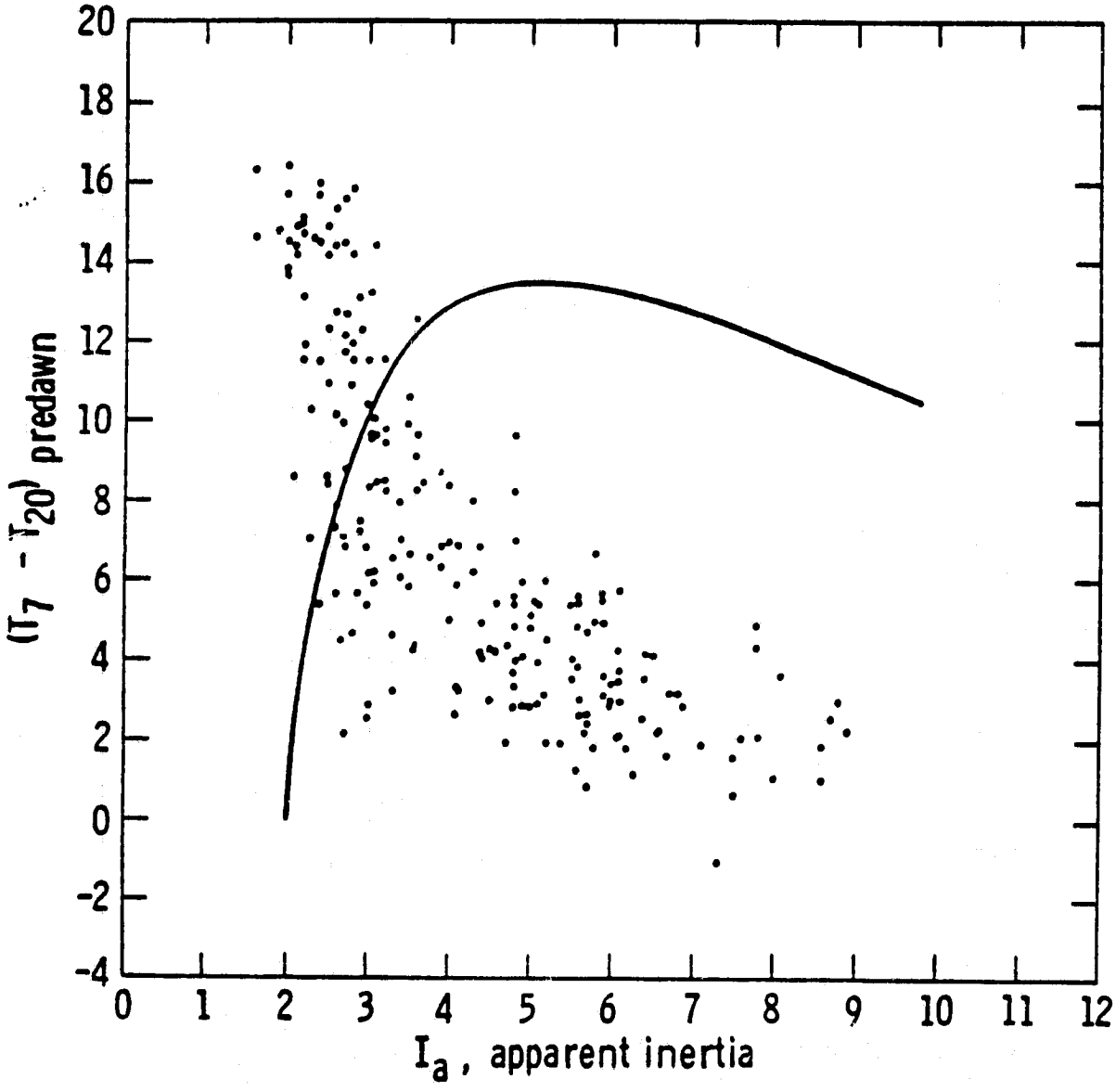
20
18
16
14
12
10
8
6
4
2
0
-2
-4
0
1
2
3
4
5
6
7
8
9
10
11
12
$(T_7 - T_{20})$ predawn
I_a, apparent inertia

Fig. 8

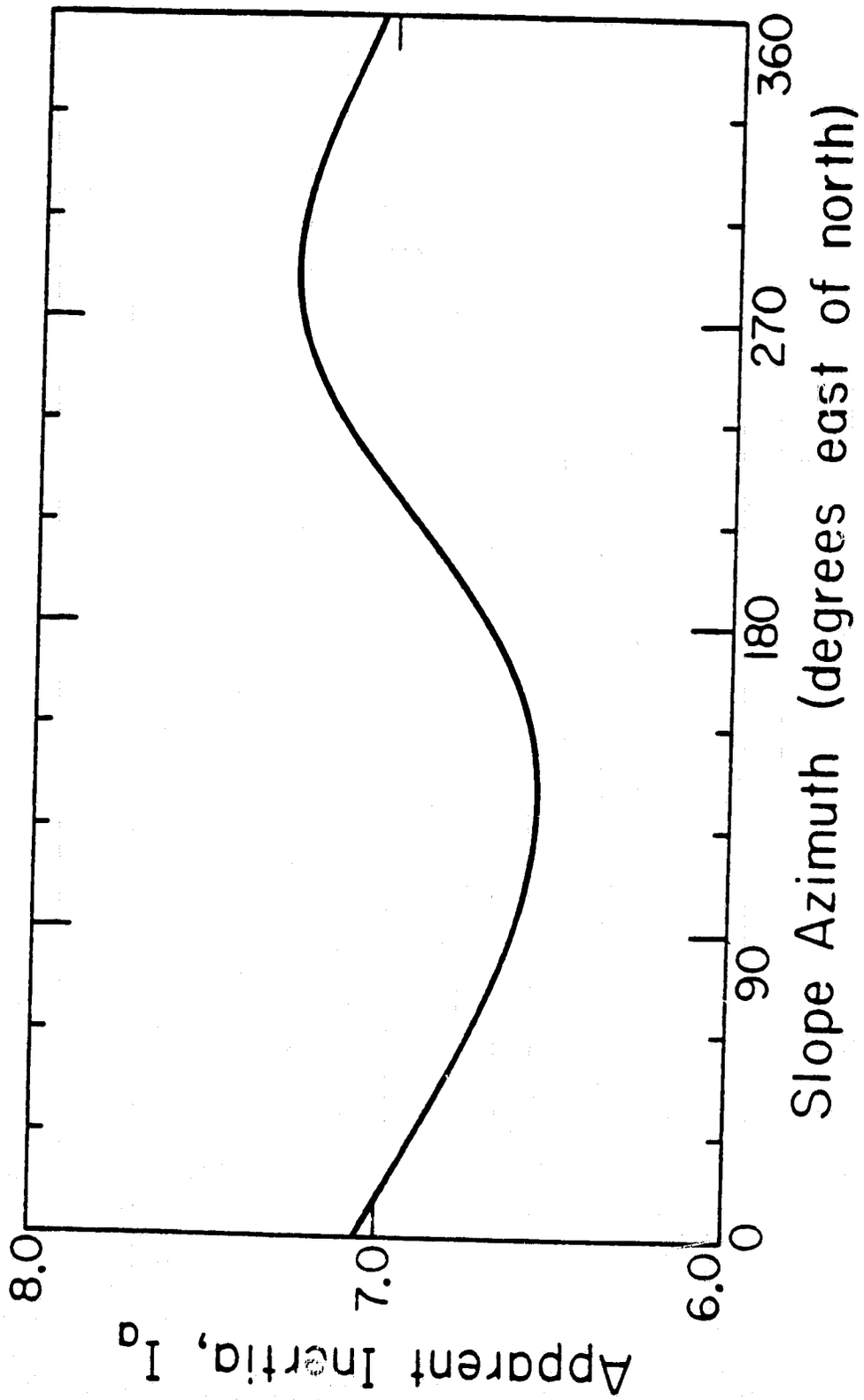
Apparent Inertia, I_a
8.0
7.0
6.0
0
90
180
270
360
Slope Azimuth (degrees east of north)

Fig. 9

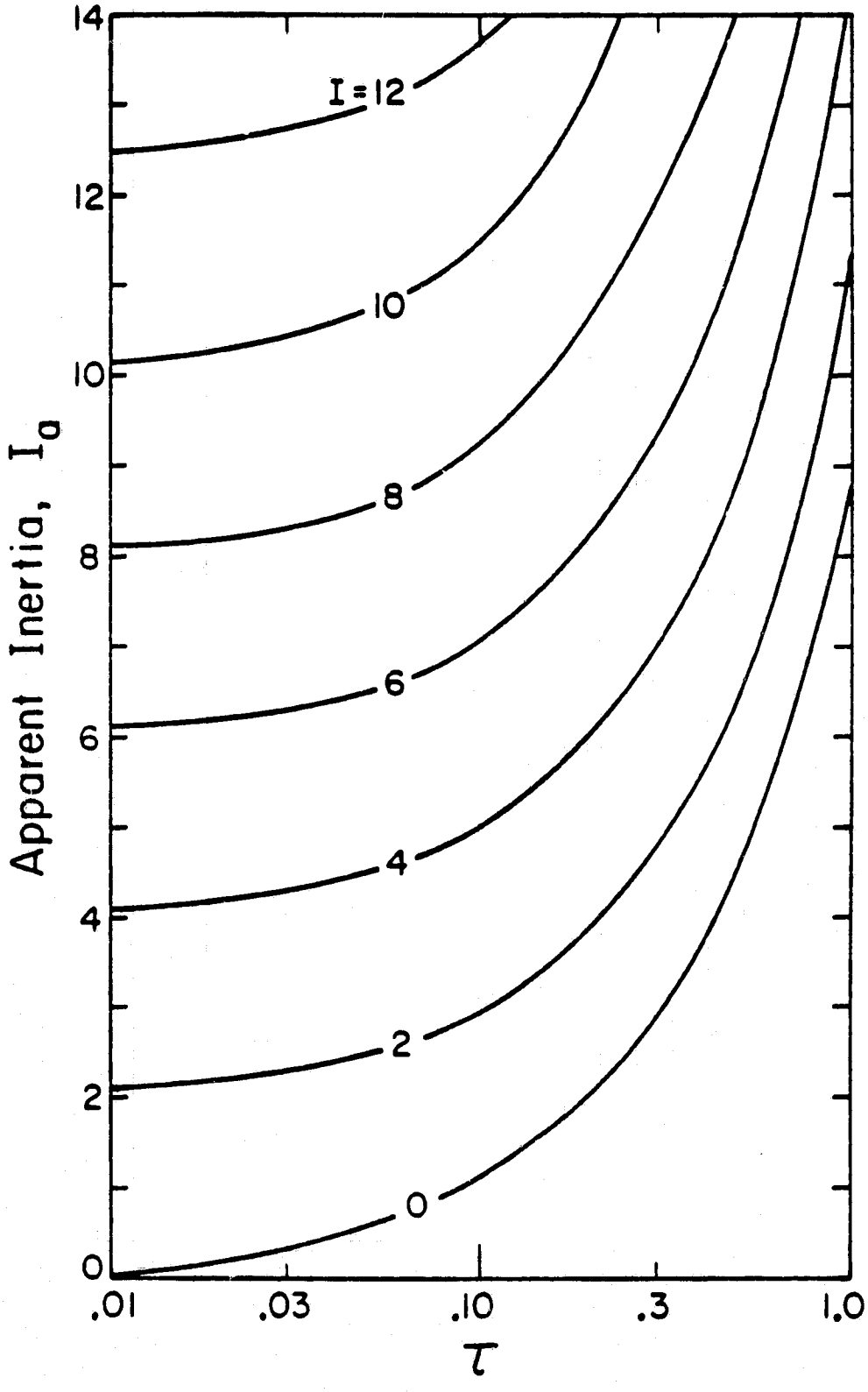
Apparent Inertia, I_a
14
12
10
8
6
4
2
0
I=12
10
8
6
4
2
0
.01
.03
.10
.3
1.0
τ

Fig. 10

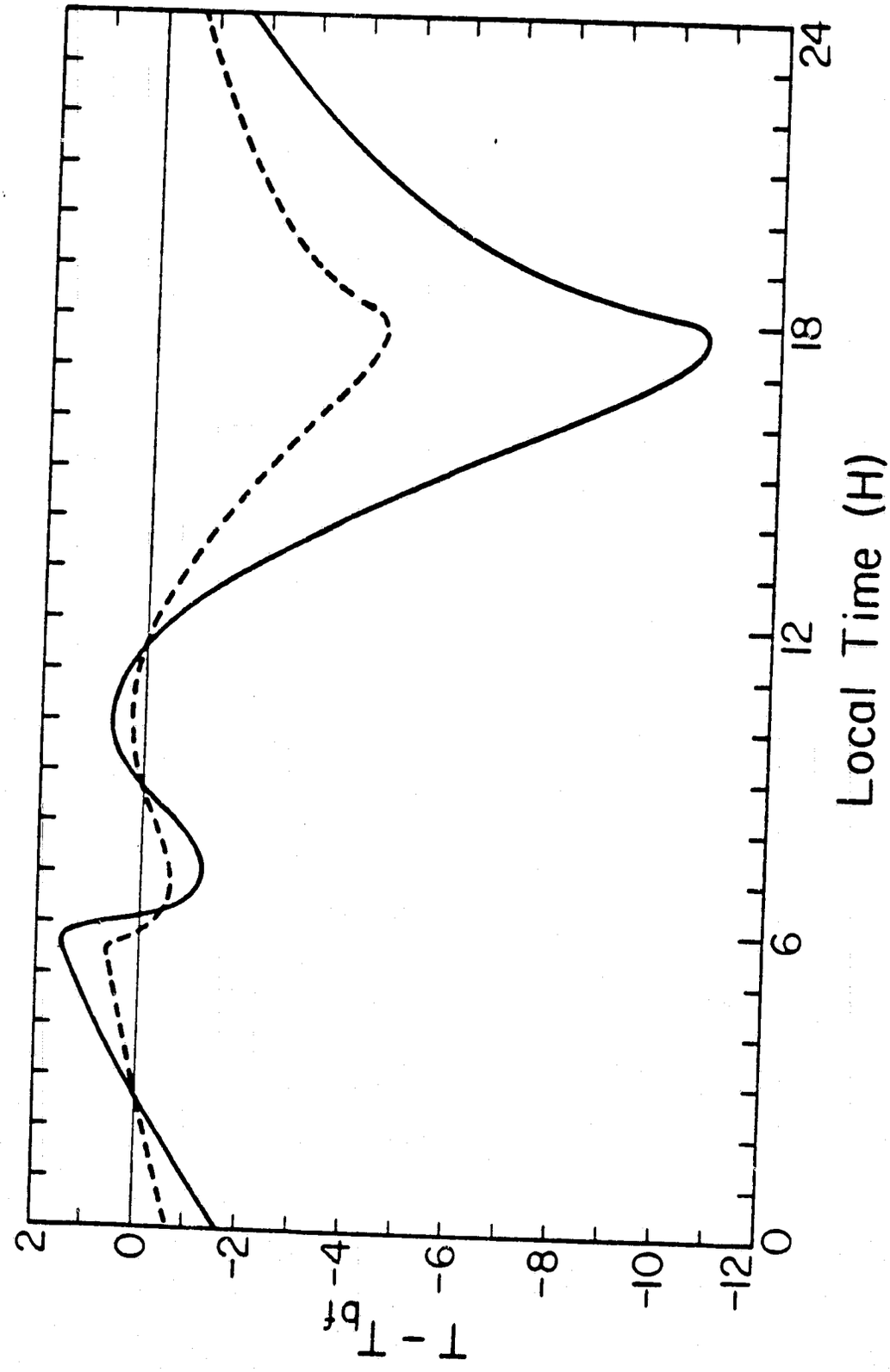

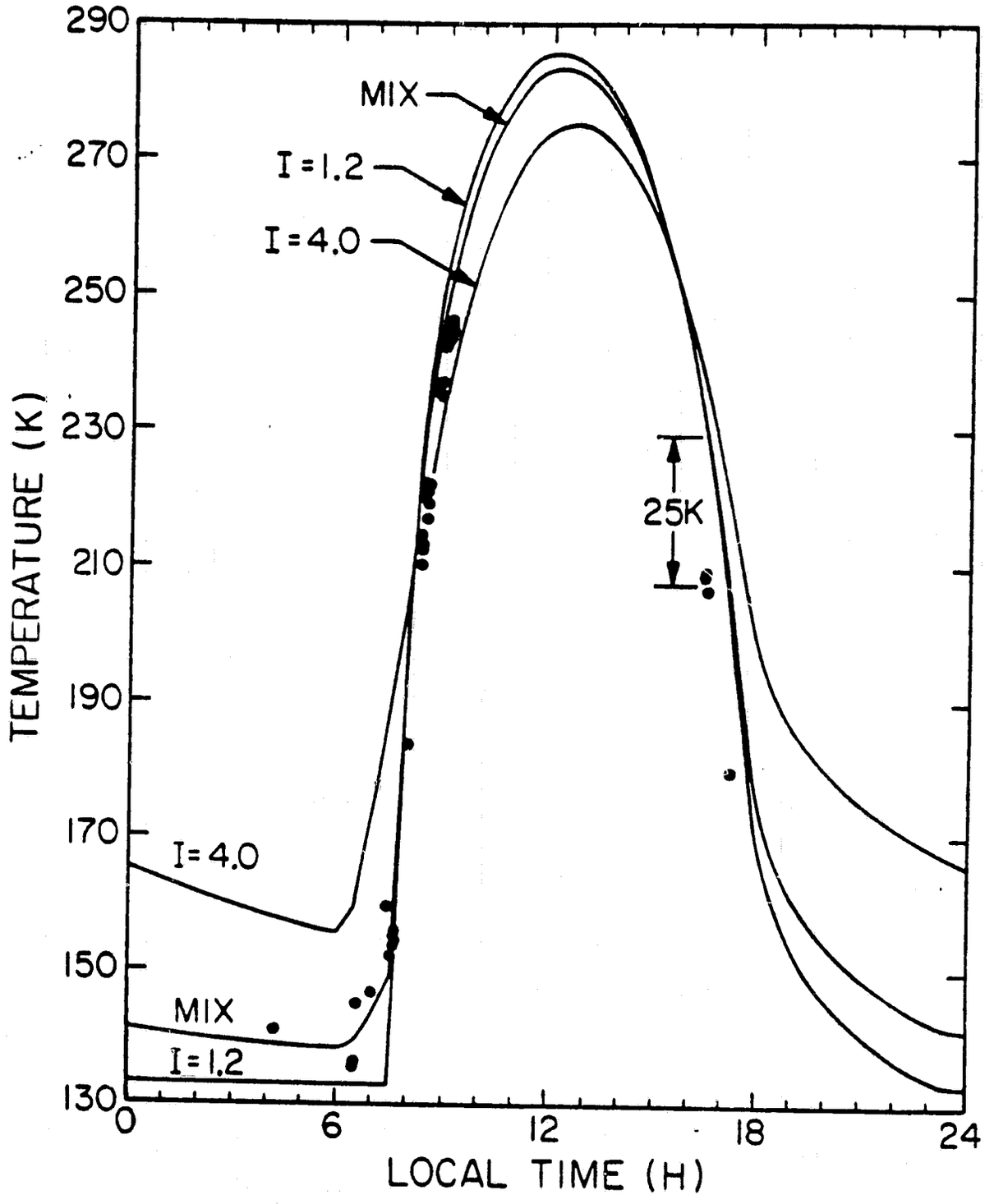
290
270
250
230
210
190
170
150
130
TEMPERATURE (K)
0
6
12
18
24
LOCAL TIME (H)
MIX
I = 1.2
I = 4.0
25K
I = 4.0
MIX
I = 1.2

Fig. 12

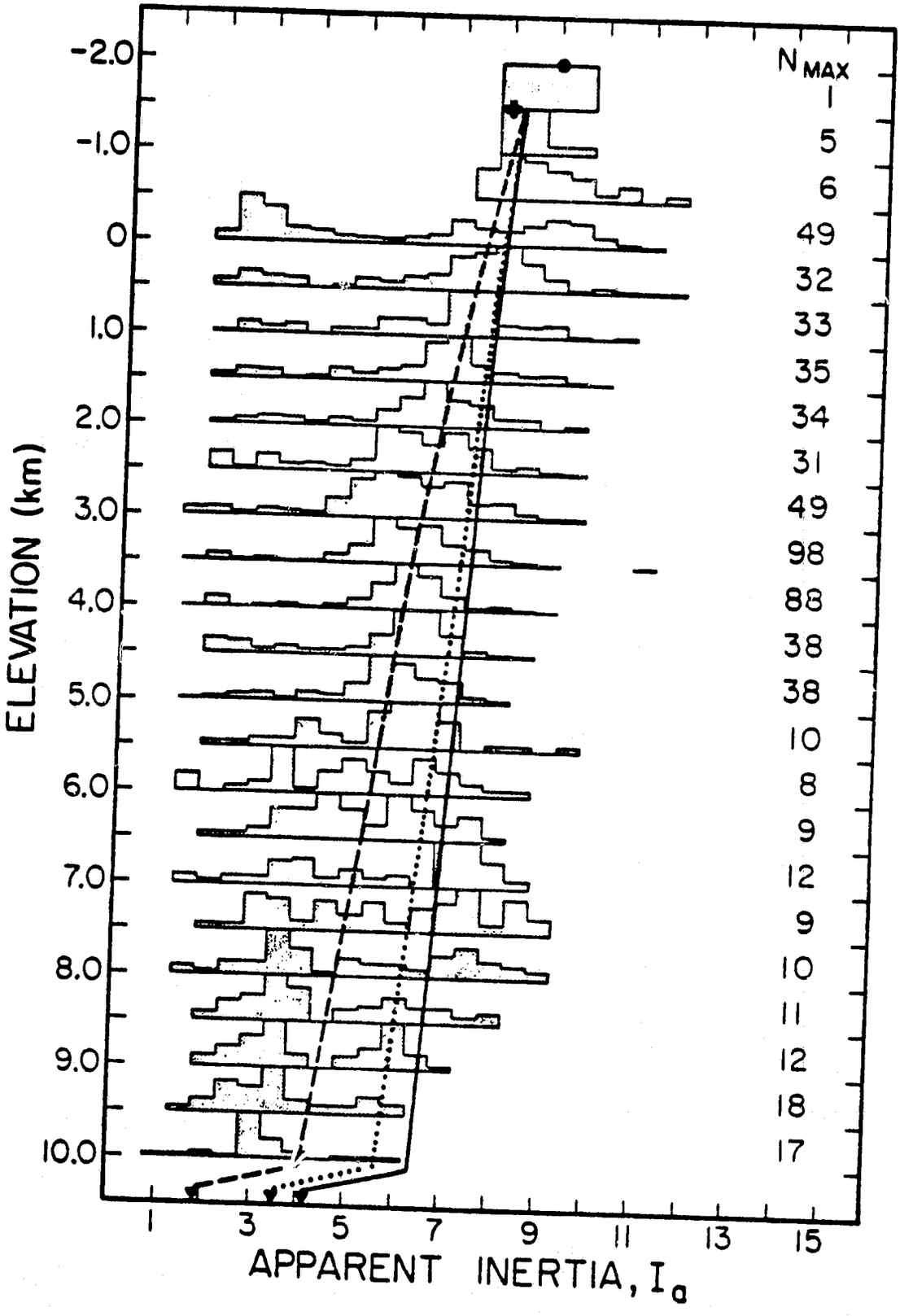
-2.0
-1.0
0
1.0
2.0
3.0
4.0
5.0
6.0
7.0
8.0
9.0
10.0
ELEVATION (km)
N MAX
1
5
6
49
32
33
35
34
31
49
98
88
38
38
10
8
9
12
9
10
11
12
18
17
1
3
5
7
9
11
13
15
APPARENT INERTIA, I_a